RESEARCH ARTICLE

Synthesis, Characterization, Magnetic Properties and Photocatalytic Activity of M-Type $BaGd_xAl_xCr_xFe_{(12-3x)}O_{19}$ Hexagonal Ferrites

Zahra.Pakdel [1], Mohammad Yousef i [2,], Malak Hekmati [3], Maryam Bikhof Torbati [4]*

[1] *Department of Chemistry, Science and Research Branch, Islamic Azad University, Tehran, Iran*

[2] *Department of Chemistry, Faculty of Pharmaceutical Chemistry, Tehran Medical Sciences, Islamic Azad University, Tehran, Iran*

[3] *Department of Organic Chemistry, Faculty of Pharmaceutical Chemistry, Tehran Medical Sciences, Islamic Azad University, Tehran, Iran*

[4] *Department of Biology, Yadegar-e- Imam Khomeini Shar-e Rey Branch, Islamic Azad University, Tehran, Iran*

ARTICLE INFO

Article History:

Received 2023-07-23

Accepted 2024-06-12

Published 2023-05-05

Keywords:

Hexagonal Ferrites,

Photocatalytic,

Sol- gel,

Magnetic.

ABSTRACT

In this study, $BaGd_xAl_xCr_xFe_{(12-3x)}O_{19}$ (x = 0.0, 0.2, 0.4, 0.6, 0.8) hexagonal ferrites were synthesized by sol-gel combustion methods. The sample X-ray diffraction pattern shows a hexagonal phase that was identified using JCPDS data (00-033-1340) and had hexagonal crystal symmetry in space group P63/MMC. On the FT-IR spectrum of $BaGd_xAl_xCr_xFe_{(12-3x)}O_{19}$, the bands at 431-605$cm^{-1}$ correspond to the Fe-O stretching vibrations and prove the formation of nanohexagonal ferrites. Field emission scanning electron microscopy (FE-SEM) pictures have represented the formation of hexagonal nanoparticles, but by increasing the dopants, which have less magnetic properties than iron (III) ions, the hexagonal structure can be seen well yet. A vibrating sample magnetometer (VSM) shows the Ms value of the barium hexaferrite (BHF) sample at approximately 63.76 emu/g, which is proportional to the predicted value for standard hexaferrites, and Hc at approximately 7000 Oe, confirming the magnetic hardness of the nanocomposite. The hysteresis diagrams show that the values of Ms and Hc decrease with increasing dopants. The degradability of methylene blue (MB) demonstrates that all samples have desirable photocatalytic properties in visible light. The degradability rates in all samples are 65%-99%. The results indicate that the degradability rate increases significantly as the dopant ions increase.

How to cite this article

Pakdel Z.,Yousefi M., Hekmati M., Bikhof Torbati M., Synthesis, Characterization, Magnetic Properties and Photocatalytic Activity of M-Type $BaGd_xAl_xCr_xFe_{(12-3x)}O_{19}$ Hexagonal Ferrites. *J. Nanoanalysis., 10 (2): 515-524, Spring 2023.*

*Corresponding Author Email: *myousefi50@hotmail.com*

INTRODUCTION

In recent years, M-type barium hexagonal ferrites (Ba-M) have been extensively used for ferrofluids due to their fabulous magnetic properties, such as high saturation magnetization, acceptable coercivity, magnetic resonance frequency, and good permeability based on their microstructures. These desirable characteristics can also make them suitable for high-density magnetic recording media and radar-absorbing materials. Also, due to its good chemical stability, corrosion resistivity, and superior magnetic properties, water purification, and photo catalysts, it has received a lot of attention [1].

The magnetoplumbite structure of Ba-M also contains 24 Fe^{3+} ions located in five sites, of which three are octahedral (12k, 2a, and 4f2) sites and two have remained for tetrahedral (4f1) and bipyramidal (2b) ones. Besides, there are various reports on the magnetization of hexagonal ferrites with different inserted cations and their combinations, such as La^{3+}, Co^{2+}, Zn^{2+}, Sn^{4+}, La^{3+}, Nd^{3+}, Ce^{3+}, Co-Zr, etc., that can affect magnetization. According to these studies, Nd^{3+} prefers to sit at 12k (↑) and 2b (↓) sub-lattices that can decrease M_S [2]. There are other classes of materials, such as dielectric oxides and superconducting oxides that are also promising for practical uses. The magnetic properties of ferromagnetic materials are similarly related to five sub-lattice spin directions, in which 12k, 2a, and 2b are up-spinning while 4f1 and 4f2 are down ones. However, the magnetization structure of synthesized magnetoplumbite is defined as depending on substituting up or down spins [3].

Various methods can be used for synthetic nanoparticles, such as co-precipitation, sol-gel auto-combustion [4], hydrothermal, ultrasonic-assisted sol-gel [5], etc. Among the synthesis methods, sol-gel auto-combustion has several benefits, such as time savings, lower prices, and the preparation of particles in a narrow particle size distribution.

M-type ferrites are good candidates for technical applications owing to their good magnetic properties and high Curie temperature. Ba-M has been used in many applications, such as super capacitors, permanent magnets, microwave filters, magnetic recording, photocatalysts, and so on, due to their high chemical stability, relatively good magnetism, and low price [6]. Investigations in recent years have shown that Ba-M hexaferrite, one of the hard-magnetic materials with high crystalline magnetic anisotropy along the c-axis, can be transformed into a soft magnetic material with planar crystalline magnetic anisotropy by doping ions with different cations such as Fe^{3+}, Ti^{4+}, Co^{2+}, Li^{+}, and Ce^{4+}. Many attempts have been made to improve the intrinsic Ba-M magnetic properties, such as magneto-crystalline anisotropy and saturation magnetism, with the substitution of cations such as Zr^{4+}, Ce^{4+}, Zn^{2+}, Co^{2+}, Ni^{2+}, etc. Moreover, there are various reports on the magnetization of hexagonal ferrites with various doped elements and their combinations, such as La^{3+}, Co^{2+}, Zn^{2+} [7, 8], Sn^{4+}, La^{3+} [9], Nd^{3+}, Cr^{3+}, Co-Zr [10], etc., that can affect the structure and magnetization. Recently, studies of the Fe^{3+} and Sr^{2+} substitution with metal and rare alkali ions have been done to improve different properties.

Despite various studies that have investigated the structural and magnetic properties of barium hexaferrite, more investigations are required to achieve practical results. In this study, $BaGd_xAl_xCr_xFe_{(12-3x)}O_{19}$ ((x=0, 0.2, 0.4, 0.6, 0.8) were synthesized via the sol-gel auto-combustion method. The photocatalytic properties of synthetic samples were evaluated under visible light. In addition, VSM, FT-IR, XRD, and FE-SEM were used to investigate the effect of adding ions on the structures and magnetic properties.

EXPERIMENTAL

Materials and Characterization

In the present study, ferric nitrate ($Fe(NO_3)_3{\cdot}9H_2O$) (Merck, 99.98% pure), $Ba(NO_3)_2.6H_2O$ (Merck, 99.98%), Al $(NO_3)_3$. $9H_2O$

(99%, Sigma Aldrich), $Gd(NO_3)_3.6H_2O$, $Cr(NO_3)_3.9H_2O$, citric acid, ammonium hydroxide, and methylene blue dye were purchased from Sigma-Aldrich Company and used without any purification. The aimed nanoparticles were prepared with the sol-gel auto-combustion method.

Fourier transform infrared spectroscopy (FT-IR) was carried out by a Bruker spectrophotometer (model 1430) at room temperature, with a spectra range of 400–4000 cm^{-1}. The X-ray diffraction pattern was recorded by a Philips- X′Pert Pro X-ray diffractometer, using Cu-Kα radiation (λ=1.5406 Aº) in the range of 2ɵ=10-80º, with a step scan of 2◦/min to determine the phase of hexaferrites.

The magnetic properties were measured by a vibrating sample magnetometer (VSM) at an applied magnetic field of ±15 kOe (measured by Magnates Daghigh Kavir Iran Co.). Particle morphology was determined by the field emission scanning electron microscope (FE-SEM, ZIES, and VP 500). Photo degradation of nanoparticles was studied by UV- Vis (λ = 200-800 nm).

Preparation of Hexaferrites

Synthesis of $BaFe_{12}O_{19}$ (A_0) nanoparticles

The nanoparticles were synthesized by the sol–gel auto-combustion method. For the Synthesis of $BaFe_{12}O_{19}$ (A_0, see **Table 1**) as the first step, 1.023 g of Ba $(NO_3)_2$, 18.97 g of Fe $(NO_3)_3{\cdot}9H_2O$, and 12.83 g of citric acid dissolved in 200 mL deionized water. Subsequently, the mixture was heated at 60 ◦C for 2 h; then the pH of the reaction mixture was adjusted at 7–8 by adding ammonia solution in a dropwise manner. After two hours, the temperature of the homogenous solution was raised to 100 ◦C and mixed for 2 h by continuous stirring to evaporate the excess water. The obtained dark green gel was heated to 200 ◦C, leading to the formation of a brown powder by the auto-combustion reaction. To eliminate organic components, the resultant fluffy mass was heated at 550 ◦C for 4 h; finally, the sample was annealed at 900 ◦C for 2 h to obtain $BaFe_{12}O_{19}$ (A_0) nanoparticles.

Preparation of A_1

A_1 was synthesized by adding 1.022 g of Ba $(NO_3)_2.6H_2O$ and 0.352 g of Gd $(NO_3)_3$ $.6H_2O$, 0.352 g of Al $(NO_3)_3$. $9H_2O$, 0.313 g of Cr $(NO_3)_3.9H_2O$, 18.016 g of Fe $(NO_3)_3$, and 11.724 g of citric acid to 200 mL of deionized water. The synthesis of other substances was the same by adding stoichiometric amounts of compounds and via sol-gel auto-combustion.

Photocatalysis

0.1 g of each sample (A_0, A_1, A_2, A_3, A_4) as a photocatalyst was dispersed in 50 mL (10mg/L) of MB solution by ultrasonication for about 15 min and stirred under dark situation around 30 min to gain adsorption-desorption equilibrium. Then, the samples were irradiated under a visible light source (the Hg-UV lamp, λ>400 nm). To prevent the temperature from increasing, the experiments were performed at room temperature (25°C) in the presence of a cool water jacket. At certain intervals (every 10 minutes), the samples were taken out and filtered. Then, the products were investigated by UV-Vis spectrophotometer. The photo degradation efficiency of the prepared samples was measured by the MB absorbance (λ max: 663 nm) at 0-60 min on the surface of the catalyst.

RESULTS AND DISCUSSION

Structural and morphological analysis

X-ray Diffraction spectroscopy (XRD)

X-ray diffraction pattern of nanocomposites are given in **Fig.1.** The pattern of samples displays hexagonal phase that was identified with the JCPDS data (00-033-1340) and had hexagonal crystal symmetry in space group P63/MMC. The observed secondary phase (small reflection at 2ɵ=26.5, 27.3, and 32.3) can be identified as α-Fe_2O_3 impurities (clarified by the star (*)).

The lattice parameters (*a, c)* and unit cell volume (V_{cell}) were calculated by the following

equations [11], Where d_{hkl} denotes the XRD pattern interplanar spacing and h,k,l denotes Miller indices.

$$\frac{1}{d^2_{hkl}} = \frac{4(h^2+hk+k^2)}{3a^2} + \frac{l^2}{c^2} \quad (1)$$

$$v_{cell} = 0.8666a^2\,c \quad (2)$$

Furthermore, the average crystallite size of the prepared sample was also calculated by the Scherer equation:

$D=0.9\,\lambda/B\cos\theta$ (3)

In which λ is the X-ray wavelength, B refers to the full width at half maximum (FWHM), and θ shows the diffraction angle. The average crystallite size of the samples (A_0, A_1, A_2, A_3 and A_4) was about 70 nm. The lattice parameters are represented in **Table 2**. Because the ionic radii of Al^{3+} and Cr^{3+} are smaller than those of Fe^{3+} (0.53 A°, 0.52 A°, and 0.64 A° respectively), the amounts of *a* and *c* were changed by inserting the dopants. Also, because of the larger ionic radii (0.93 A°) of rare-earth ions (here Gd^{3+} [12]), substitution could be limited, and by enhancing the amount of Gd^{3+} the aggregation would happen, and hexaferrite structure distortion is possible as well, which can be explained by the crystalline defects that are observed after inserting rare-earth ions. This fact can be explained by the larger ionic radii of dopants. The values of the c/a ratio are represented in the table and they are in the range of 3.91-3.98 and confirm the formation of M-type hexagonal structure unchanged [13].

The peaks also shifted to a higher 2θ as the dopants were inserted. The intensity of the peaks also changed with the decrease in hexaferrite peaks, which confirms a decline in crystallization degree [14].

Table1. Sample codes

Sample	Code
$BaFe_{12}O_{19}$	A_0
$BaGd_{0.2}Al_{0.2}Cr_{0.2}Fe_{11.4}O_{19}$	A_1
$BaGd_{04}Al_{04}Cr_{0.4}Fe_{10.8}O_{19}$	A_2
$BaGd_{0.6}Al_{0.6}Cr_{0.6}Fe_{10.2}O_{19}$	A_3
$BaGd_{0.8}Al_{0.8}Cr_{0.8}Fe_{9.6}O_{19}$	A_4

Table 2. Crystalline parameters of prepared samples

sample	Lattice constant *a* *(A°)*	Lattice constant *c* *(A°)*	unit cell volume V_{cell} $(A°^3)$	*c/a*	Crystalline size *D(nm)*
A_0	5.89	23.21	697.78	3.94	42.6
A_1	5.93	23.33	710.95	3.93	85.5
A_2	5.96	23.33	718.16	3.91	71.1
A_3	5.95	23.67	726.19	3.97	76.4
A_4	5.95	23.69	735.08	3.98	75.4

FT-IR spectrums

Fig.2 represents the FT-IR spectra of

unsubstituted and substituted hexaferrites. A (x=0, 0.2, 0.4, 0.6 and 0.8). The peaks at 431-605cm^{-1} correspond to the Fe-O stretching vibrations [15]. By comparing the bands, it can be seen that they have shifted towards longer wavelengths, which is due to the addition of Gd ions. These ions are heavier than Fe, so they move the bands to longer wavelengths. The band seen in **Fig. 2** in the range of 862 cm^{-1} is related to Ba-O vibration. A band can also be seen in the 2354 cm^{-1} area that is related to CO_2. In addition, the band at 3750 cm^{-1} can be attributed to the O-H stretching bands of water molecules.

Morphology Analysis of Powders

Morphology and chemical compositions of the prepared nano-hexaferrites $BaGd_xAl_xCr_xFe_{(12-3x)}O_{19}$ ((x=0, 0.2, 0.4, 0.6, 0.8) (A_0, A_1, A_2, A_3, A_4)) were examined by FE-SEM [16]. From the resulting micrographs, the hexagonal structure of $BaFe_{12}O_{19}$ is apparent (**Fig. 3** (a)). Likewise, by inserting dopants the microstructure changed as is apparent in **Fig.3** (b-e) [17]. It should be mentioned that the average particle size is 120 nm for A-series samples. In the self-combustion sol-gel method, the particles become porous due to the gas that comes out, and due to the magnetic nature of the particles, these nanomaterials stick together and agglomerate [4]. In example A, due to the high magnetism, the particles are slightly attached to each other, but the hexagonal structure is somewhat well visible. By increasing the dopants, which have less magnetic properties than iron (III) ions, the hexagonal structure can be seen well [18].

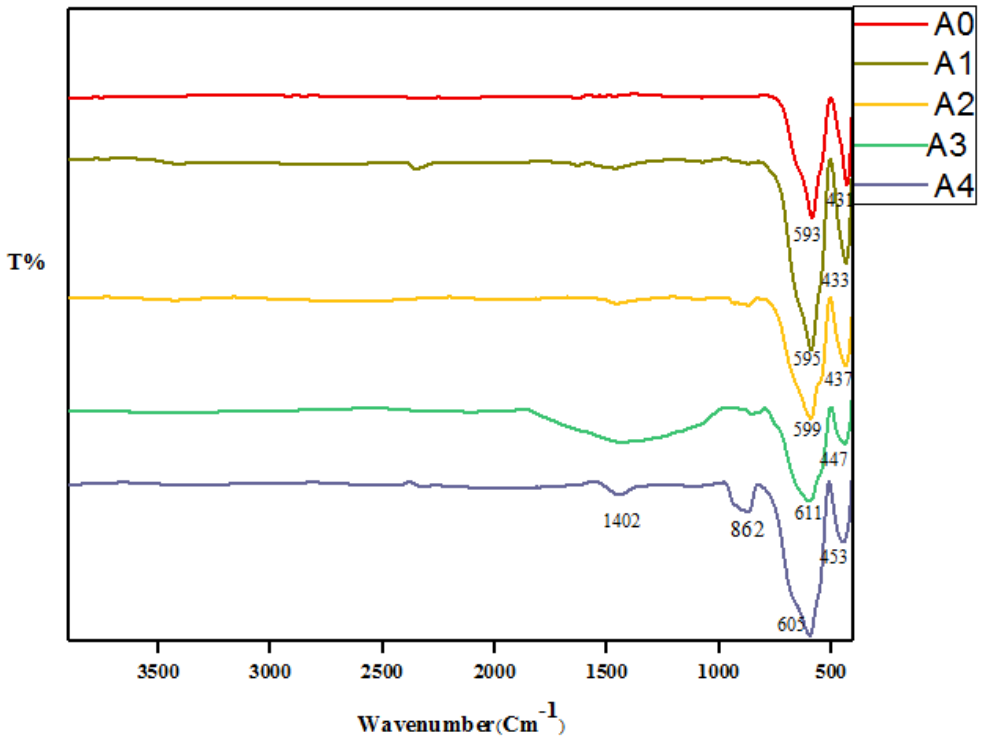

Fig.2. FT-IR spectra of $BaGd_xAl_xCr_x$ Fe $_{(12-3x)}$ O_{19} (x=0.2, 0.4, 0.6, 0.8) (A_1, A_2, A_3, A_4)

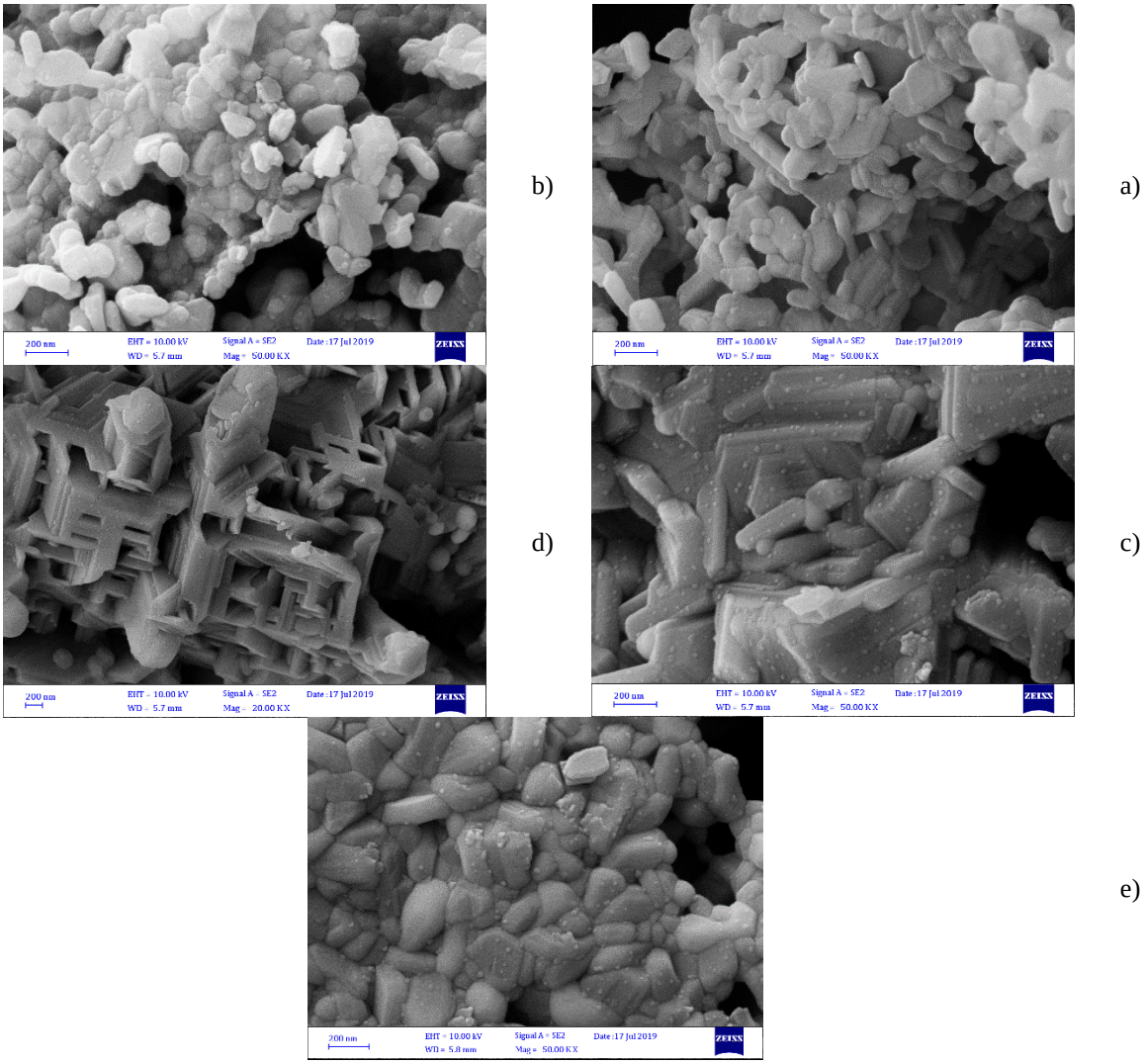

Fig.3. FE-SEM micrographs of (A_0 (a), A_1 (b), A_2 (c), A_3 (d), A_4 (e)) and EDX of (A_0, A_1, and A_4)

Magnetic Properties

The magnetic data of the synthesized nanoparticles (A_0, A_1, A_2, A_3, and A4) and the hysteresis rings of the nanocomposites are shown in in **Fig.4** and **Table 3**. The Ms value of the BHF sample is about 63.76 emu / g, which is proportional to the predicted value for standard hexaferites [19] (63 emu / g). Hc is around 7000 Oe, which confirms the magnetic hardness of the nanocomposite. The hysteresis diagrams show that the values of Ms and Hc decrease with increasing dopants. As the ions doped increases, the saturation magnet decreases and this indicates that the magnetic properties of these substituted ions are low. According to the X-ray diffraction pattern and the hysteresis diagram of the prepared samples, the magnetic residue of the prepared samples decreased with the increase of guest ions, which indicates the softness of their magnetic properties. According to Stoner-Wolfart theory, the ratio of magnetic residue to ideal saturation magnet in hexagonal ferrites is about 0.5 and confirms the existence of axial anisotropy [20].

When magnetic material is placed in the magnetic field it is observed that flux density (B) lags behind the magnetizing force that produces it, and a hysteresis loop is produced in this way [21]. Magnetic characteristics like saturation magnetization (Ms), remanence, coercivity (Hc), and squareness ratio (Mr/Ms) are estimated through hysteresis (M-H) loops. The results are introduced for the magnetic parameters of fabricated specimens in **Table 3**. Based on the

obtained hysteresis loops and magnetic characterization measurements at room temperature, saturation magnetization (Ms) of M-type strontium hexagonal ferrites was about 68.36 emu/g which was in good accordance with the expected amount.

Photocatalytic activity

The degradability rates of all substituted hexaferrites, $BaGd_xAl_xCr_xFe_{(12-3x)}O_{19}$ (x=0, 0.2, 0.4, 0.6, 0.8) (A_0, A_1, A_2, A_3, A_4), were investigated under the visible light irradiation investigation in order to confirm the photocatalytic properties of the prepared samples. The results are represented in **Fig.5.** The percentages of degradation are around 65% to 99%. According to the results, the degradation rate was considerably enhanced in A_4, which consists of larger amounts of inserting ions and confirmed the potential of substituted $BaFe_{12}O_{19}$ nanoparticles in the field of photocatalysis. The results have been calculated using the following equation:

$$D(\%) = \frac{C_0 - C}{C_0} \qquad (4)$$

C refers to the pollutant concentration (MB dye here) after adsorption and C_0 is the initial concentration of dye. Under visible light exposure, A_0 and A_1 have shown increased degradation up to 65% and 69%, respectively, in 60 minutes. Finally, the highest amount of degradation in 60 minutes is related to A_4 by 92%. UV-Vis spectra were used to study the optical absorption of A_0, A_1, A_2, A_3, and A_4. The obtained trend can be contributed to the inducing rare earth ions in the host lattice of $BaFe_{12}O_{19}$ that reduce the bandgap, consequently [22]. The irradiation of an appropriate wavelength ($h\upsilon \geq Eg$) on the surface catalytic compounds produces (e^-) and hole (h^+) pairs in the valence band [24]. Transition metals produce electrons under light irradiation, and oxygen molecules adsorb electrons and provide an unstable and energetic radical, the super dioxide anion, that ultimately reacts with contaminant molecules (here dye) and degrades them constantly. On the other hand, the fabricated super dioxide ions can react with H^+ frequently to prepare H_2O_2 which immediately decomposes and creates other impermanent degrading species of OH^- that continues the degradation of pollutants. Ultimately, after electron excitation, the positive holes (h^+) react with water molecules and form OH^- to minimize MB solution [9, 25].

$A_4 + h\upsilon$ (visible light) $\rightarrow A_4^*(h^+ + e^-$ obtained in CB and VB, respectively)

$O_2 + e^- \rightarrow O_2^{\cdot -}$

$O_2^{\cdot -} + H^+ \rightarrow O_2 + H_2O_2$

$H_2O_2 \rightarrow 2OH^-$

$H_2O + h^+ \rightarrow OH^- + H^+$

$MB + OH^- \rightarrow$ Degradation products ($CO_2 + H_2O$)

$MB + O_2^{\cdot -} \rightarrow CO_2 + H_2O$

The first-order photodegradation kinetic curves of synthesized photocatalysts are represented in **Fig. 6** for a better understanding of the degradation process of MB dye and plotted according to $\mathrm{Ln}\left(C/C_0\right) = \mathrm{K.t}$ versus irradiation time (min). C_0 is initial and C refers to after exposure light concentration respectively; K and t are first-order rate constants and exposure times as well [26]. The kinetic constants (K) are presented in **Table 4** that concern all specimens that follow first-order kinetics based on the mechanism. The kinetic constants (K) illuminate A_4 represent better MB degradation among all synthesized catalysts. Although after introducing photocatalysts to the color solution for 30 minutes the concentration of dye decreased, in the case of B_4 this decrease is more visible which can be explained by the increasing foreign ion ratios, which, as mentioned result in a decreasing band gap. To evaluate the stability of $BaGd_xAl_xCr_xFe_{(12-3x)}O_{19}$ (x=0, 0.2, 0.4, 0.6, 0.8) (A_0, A_1, A_2, A_3, A_4), reusability was measured by repeating the experiment for three times at a controlled temperature. For this purpose, after collecting catalyst agents magnetically, filtered and washed every time, the recycled catalysts were reused in the same experimental condition, and the reusability data are

shown in **Table 4**. Although the photocatalytic activity of agents is deceased, they have represented efficient degradation of about 85% for A_4 after 3 times reusing. In conclusion, A_4 represented the best photo degradation even after 3-time recycling usage.

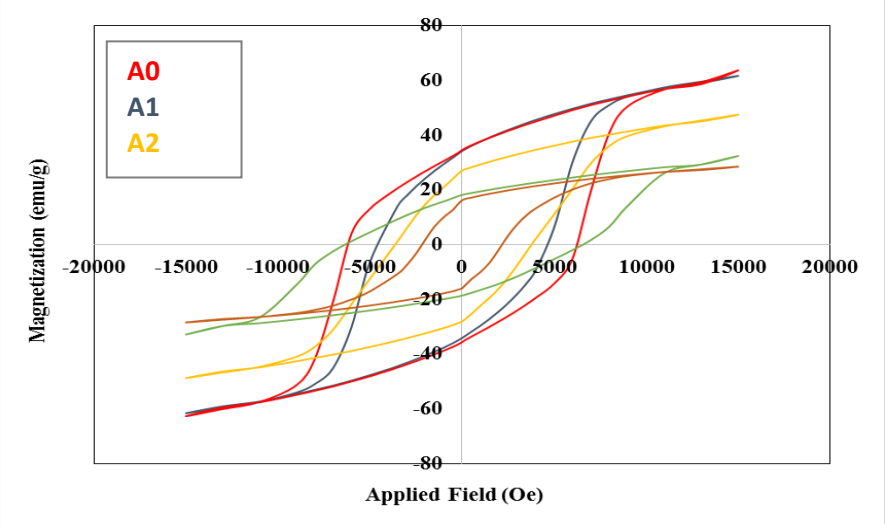

Fig.4. Magnetic hysteresis loops for the composite samples of BaGdxAlxCrx Fe $_{(12-3x)}$ O_{19} ((x=0, 0.2, 0.4, 0.6, 0.8) (A_0, A_1, A_2, A_3, A_4))

Table 3. Magnetic parameters of $BaGd_xAl_xCr_x$ Fe $_{(12-3x)}$ O_{19} ((x=0, 0.2, 0.4, 0.6, 0.8) (A_0, A_1, A_2, A_3, A_4))

Sample	M_s(emu/g)	H_C(Oe)	M_r	M_r/M_S
A_0	63.76	7000	34.6	0.54
A_1	62	5000	34.6	0.55
A_2	47.54	4000	27.09	0.56
A_3	32.45	7000	17.22	0.53
A_4	28.56	2000	16.26	0.56

Table 4. The photo degradation parameter of fabricated specimens

Sample	**Kinetic constants K(min^{-1})**	**Degradation Rate (%)**	**Reusability**		
			Recycle Time (min) 1	**Recycle Time (min) 2**	**Recycle Time (min) 3**
A_0	0.023	69	59	57	53
A_1	0.038	70	67	64	61
A_2	0.050	77	65	63	60
A_3	0.068	85	81	79	77
A_4	0.084	92	89	87	84

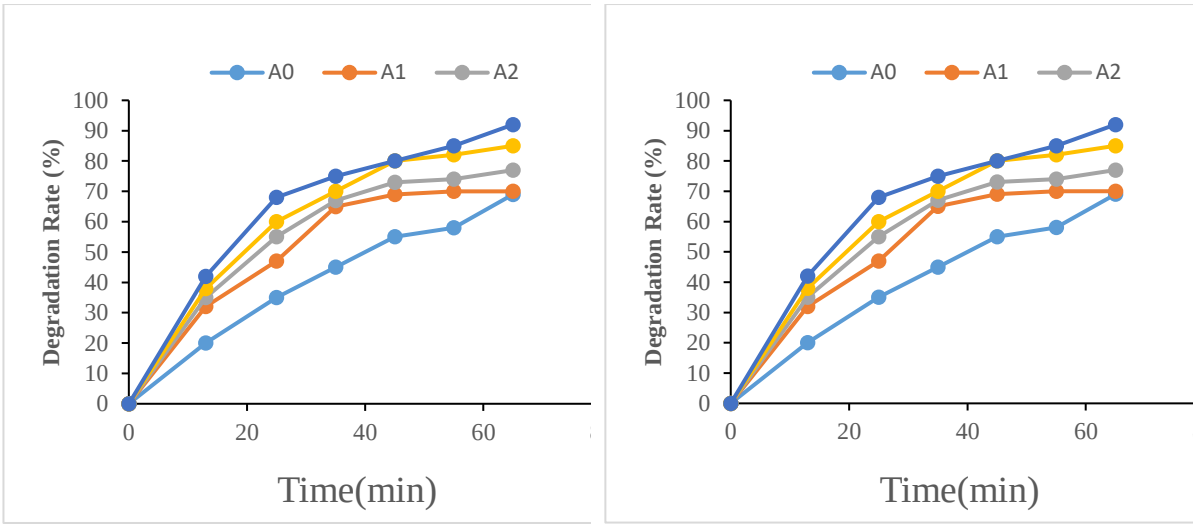

Fig.5. Degradation rate of samples (A_0, A_1, A_2, A_3, A_4)

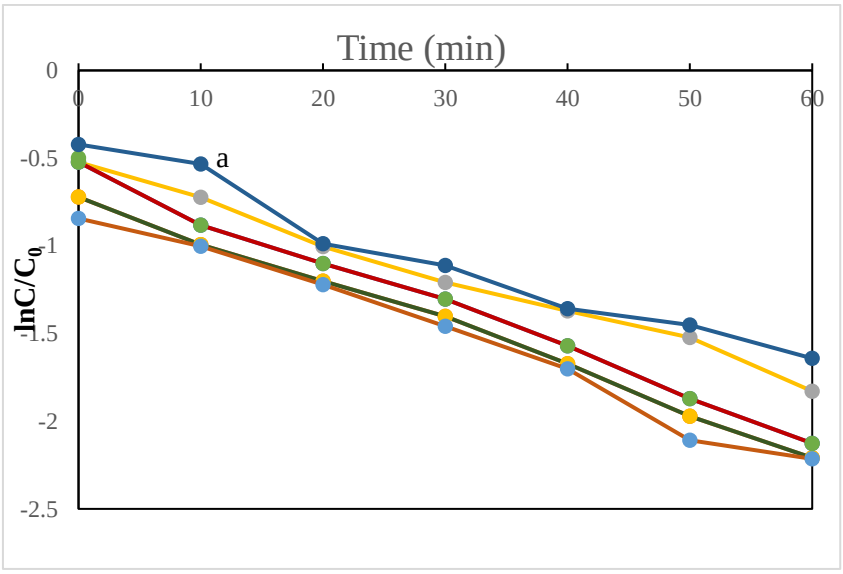

Fig.6. Kinetic plots of (ln C/C_0) versus exposure time of a) A_0, b) A_1, c) A_2, d) A_3 and e) A_4

CONCLUSION

In conclusion, this study attempts to investigate the effects of inducing ions (Gd^{3+}, Al^{3+} and Cr^{3+}) on the chemical structure, morphology, magnetic structure, and photocatalytic properties of prepared samples under visible light. In the X-ray diffractometer, by inserting ions the values of the c/a ratio were in the range of 3.91-3.98, which confirms the M-type hexagonal structure.

FE-SEM images represented the formation of hexagonal nanoparticles; besides, their average particle size was around 120 nm. A magnetization study showed that by substituting dopants in the hexaferrite structure, Ms and Hc were reduced. The photocatalytic activity of samples was measured for removing MB under visible light, and the consequences approved that adding higher dopant ions considerably increased the percentages of degradation. The results confirmed the potential of M-type $BaGdxAlxCrxFe_{(12-3x)}$ O19 hexagonal ferrites nanoparticles in the field of photocatalytic degradation in visible light.

ACKNOWLEDGMENT

The authors would like to express their appreciation to the Science and Research Branch of Islamic Azad University for their technical support.

REFERENCES

[1] Mesdaghi S, Yousefi M, Sadr MH, Mahdavian A. Effect of Sn^{4+}–Zn^{2+}–Co^{2+} Doping on Structural and Magnetic Properties of M-Type Barium Hexaferrites. IEEE Transactions on Magnetics. 2018; 55(1):1-6.

[2] Ghezelbash S, Yousefi M, Hossainisadr M, Baghshahi S. Structural and magnetic properties of Sn^{4+} doped strontium hexaferrites prepared via sol–gel auto-combustion method. IEEE Transactions on Magnetics. 2018; 54(9):1-6.

[3] Tavakolinia F, Yousefi M, Afghahi SSS, Baghshahi S, Samadi S. Synthesis of novel hard/soft ferrite composites particles with improved magnetic properties and exchange coupling. Processing and Application of Ceramics. 2018; 12(3):248-256.

[4] Almessiere MA, Slimani Y, Gungunes H, Sertkol M, Nawaz M, Algarou NA, Baykal A, Ercan I. Tb^{3+} substituted strontium hexaferrites: structural, magnetic and optical investigation and cation distribution. Journal of Rare Earths. 2020; 38(4):402-410.

[5] Almessiere MA, Slimani Y, Korkmaz AD, Güner S, Maarouf A, Baykal A. Comparative study of sonochemically synthesized Co-Zr and Ni-Zr substituted Sr-hexaferrites: magnetic and structural investigations. Journal of Magnetism and Magnetic Materials. 2020; 497:165996.

[6] Mesdaghi S, Yousefi M,Mahdavian A. The effect of PANI and MWCNT on magnetic and photocatalytic properties of substituted barium hexaferrite nanocomposites. Materials Chemistry and Physics. 2019; 236:121786.

[7] Asghar G, Anis-ur-Rehman M. Structural, dielectric and magnetic properties of Cr–Zn doped strontium hexa-ferrites for high frequency applications. Journal of alloys and compounds. 2012; 526:85-90.

[8] Ashiq MN, Shakoor S, Najam-ul-Haq M, Warsi MF, Ali I, Shakir I. Structural, electrical, dielectric and magnetic properties of Gd-Sn substituted Sr-hexaferrite synthesized by sol–gel combustion method. Journal of Magnetism and Magnetic Materials. 2015; 374:173-178.

[9] Kumar P, Chand P, Joshi A, Luxmi V,Singh V. Rare earth substituted Bi0. 84RE0. 16FeO3 (RE= La, Gd)-an efficient multiferroic photo-catalyst under visible light irradiation. International Journal of Hydrogen Energy. 2020; 45(34):16944-16954.

[10] Pakdel Z, Yousefi M, Hekmati M, Torbati MB. The effect of dopped Al^{3+}-Gd^{3+}-Cr^{3+} on the chemical structure of M− type strontium hexaferrite and investigation on their photocatalysis properties. Inorganic Chemistry Communications. 2021; 134:108969.

[11] Shlyk L, Vinnik D, Zherebtsov D, Hu Z, Kuo C-Y, Chang C-F, Lin H-J, Yang L-Y, Semisalova A, Perov N. Single crystal growth, structural characteristics and magnetic properties of chromium substituted M-type ferrites. Solid State Sciences. 2015; 50:23-31.

[12] Iorgu A, Maxim F, Matei C, Ferreira LP, Ferreira P, Cruz M, Berger D. Fast synthesis of rare-earth (Pr3+, Sm3+, Eu3+ and Gd3+) doped bismuth ferrite powders with enhanced magnetic properties. Journal of Alloys and Compounds. 2015; 629:62-68.

[13] Ali I, Islam M, Awan M, Ahmad M. Effects of Ga–Cr substitution on structural and magnetic properties of hexaferrite (BaFe12O19) synthesized by sol–gel auto-combustion route. Journal of Alloys and Compounds. 2013; 547:118-125.

[14] Sharma S, Satyapal HK, Kumar SS, Aryan R, Manash A, Kumar V. Effect of Gd3+ substitution on the structural and magnetic properties of barium hexaferrite nanomaterials. Materials Today: Proceedings. 2021; 44:2587-2592.

[15] Almessiere MA, Slimani Y, Tashkandi N, Baykal A, Saraç MF, Trukhanov A, Ercan İ, Belenli İ,

Ozçelik B. The effect of Nb substitution on magnetic properties of BaFe12O19 nanohexaferrites. Ceramics International. 2019; 45(2):1691-1697.

[16] Slimani Y, Selmi A, Hannachi E, Almessiere MA, Mumtaz M, Baykal A, Ercan I. Study of tungsten oxide effect on the performance of BaTiO 3 ceramics. Journal of Materials Science: Materials in Electronics. 2019; 30:13509-13518.

[17] López-Ortega A, Lottini E, Fernandez CdJ, Sangregorio C. Exploring the magnetic properties of cobalt-ferrite nanoparticles for the development of a rare-earth-free permanent magnet. Chemistry of materials. 2015; 27(11):4048-4056.

[18] Slimani Y, Baykal A, Amir M, Tashkandi N, Güngüneş H, Guner S, El Sayed H, Aldakheel F, Saleh TA, Manikandan A. Substitution effect of Cr^{3+} on hyperfine interactions, magnetic and optical properties of Sr-hexaferrites. Ceramics International. 2018; 44(13):15995-16004.

[19] Smail S, Benyoussef M, Taïbi K, Bensemma N, Manoun B, El Marssi M, Lahmar A. Structural, dielectric, electrocaloric and energy storage properties of lead free Ba0. 975La0. 017 (ZrxTi0. 95-x) Sn0. 05O3 (x= 0.05; 0.20) ceramics. Materials Chemistry and Physics. 2020; 252:123462.

[20] Xu M, Zhang J, Wang S, Guo X, Xia H, Wang Y, Zhang S, Huang W, Wu S. Gas sensing properties of SnO2 hollow spheres/polythiophene inorganic–organic hybrids. Sensors and Actuators B: Chemical. 2010; 146(1):8-13.

[21] Afghahi SSS, Jafarian M, Atassi Y, Stergiou CA. Single and double-layer composite microwave absorbers with hexaferrite BaZn0. 6Zr0. 3X0. 3Fe10. 8O19 (X= Ti, Ce, Sn) powders. Materials Chemistry and Physics. 2017; 186(584-591.

[22] Güner S, Almessiere MA, Slimani Y, Baykal A, Ercan I. Microstructure, magnetic and optical properties of Nb3+ and Y3+ ions co-substituted Sr hexaferrites. Ceramics International. 2020; 46(4):4610-4618.

[23] Xie T, Liu C, Xu L, Yang J, Zhou W. Novel heterojunction Bi2O3/SrFe12O19 magnetic photocatalyst with highly enhanced photocatalytic activity. The Journal of Physical Chemistry C. 2013; 117(46):24601-24610.

[24] Yousefi M, Afghahi S, Amini M, Torbati MB. An investigation of structural and magnetic properties of Ce–Nd doped strontium hexaferrite nanoparticles as a microwave absorbent. Materials Chemistry and Physics. 2019; 235:121722.

[25] Dhiman M, Singhal S. Effect of doping of different rare earth (europium, gadolinium, dysprosium and neodymium) metal ions on structural, optical and photocatalytic properties of LaFeO3 perovskites. Journal of Rare Earths. 2019; 37(12):1279-1287.

[26] Ahmad R, Mondal PK. Adsorption and photodegradation of methylene blue by using PAni/TiO2 nanocomposite. Journal of dispersion science and technology. 2012; 33(3):380-386.